

See discussions, stats, and author profiles for this publication at: <https://www.researchgate.net/publication/263956953>

# Topochemical Preparation of WO<sub>3</sub> Nanoplates through Precursor H<sub>2</sub>WO<sub>4</sub> and Their Gas-Sensing Performances

ARTICLE in THE JOURNAL OF PHYSICAL CHEMISTRY C · AUGUST 2011

Impact Factor: 4.77 · DOI: 10.1021/jp205782a

CITATIONS

70

READS

81

7 AUTHORS, INCLUDING:



Jianmin Ma

Hunan University

94 PUBLICATIONS 1,707 CITATIONS

SEE PROFILE



Jun Zhang

University of Jinan (Jinan, China)

163 PUBLICATIONS 2,979 CITATIONS

SEE PROFILE



Taihong Wang

Hunan University

279 PUBLICATIONS 12,362 CITATIONS

SEE PROFILE



Wenjun Zheng

Nankai University

112 PUBLICATIONS 2,308 CITATIONS

SEE PROFILE

# Topochemical Preparation of WO<sub>3</sub> Nanoplates through Precursor H<sub>2</sub>WO<sub>4</sub> and Their Gas-Sensing Performances

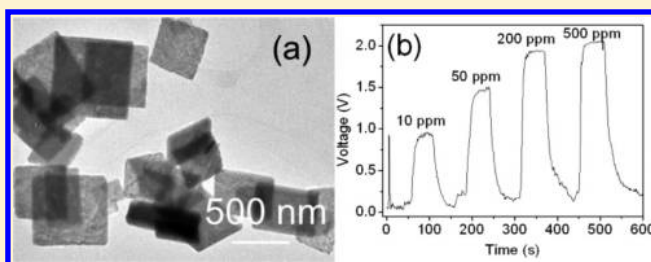
Jianmin Ma,<sup>†,‡</sup> Jun Zhang,<sup>§</sup> Shurong Wang,<sup>§</sup> Taihong Wang,<sup>†</sup> Jiabiao Lian,<sup>‡</sup> Xiaochuan Duan,<sup>‡</sup> and Wenjun Zheng<sup>†,\*</sup>

<sup>†</sup>Key Laboratory for Micro-Nano Optoelectronic Devices of Ministry of Education, State Key Laboratory for Chemo/Biosensing and Chemometrics, Hunan University, Changsha, 410082, P. R. China

<sup>‡</sup>Department of Materials Chemistry, Key Laboratory of Advanced Energy Materials Chemistry (MOE), College of Chemistry, Nankai University, Tianjin, 300071, P. R. China

<sup>§</sup>Department of Chemistry, Key Laboratory of Advanced Energy Materials Chemistry (MOE), College of Chemistry, Nankai University, Tianjin, 300071, P. R. China

**ABSTRACT:** Size- and shape-controllable preparation of WO<sub>3</sub> nanoplates has been successfully realized through topochemical transformation of corresponding H<sub>2</sub>WO<sub>4</sub> precursors synthesized by a facile solution-phase method. The fluoroboric acid was found to not only provide acid source but also act as a structure-directing agent during the growth process of H<sub>2</sub>WO<sub>4</sub> nanoplates in the solution phase. WO<sub>3</sub> nanoplates could be obtained by the two different topochemical transformation methods, hydrothermal treatment of H<sub>2</sub>WO<sub>4</sub> nanoplates at the temperature (above 160 °C) and calcination at higher temperatures in air, based on their similarity of the W–O octahedral layers in both H<sub>2</sub>WO<sub>4</sub> and WO<sub>3</sub>. Furthermore, the enhanced ethanol-sensing performance could be attributed to the plate-like morphology, especially the high crystallinity, due to the advantages of the effective adsorption and rapid diffusion of the ethanol molecules.



## 1. INTRODUCTION

The design and rational synthesis of inorganic semiconductors with tailored characteristics (dimensionality, morphology, crystal phase, components, crystallinity, etc.) have attracted increasing attention because they largely determine the physical properties of the materials.<sup>1–4</sup> As an important n-type semiconductor, tungsten trioxide (WO<sub>3</sub>) has received much attention in the past few decades owing to its intriguing physiochemical properties and widespread potential applications. Currently, WO<sub>3</sub> materials have been reported to have been used in a variety of fields, such as electrochromic and photochromic devices,<sup>5,6</sup> lithium ion batteries,<sup>7,8</sup> photocatalysts,<sup>9,10</sup> gas sensors,<sup>11–13</sup> heterogeneous catalysts,<sup>14,15</sup> solar energy devices,<sup>16,17</sup> field electron emission<sup>18,19</sup> smart windows,<sup>20</sup> superconductivity, thermoelectricity, and ferroelectric properties,<sup>21</sup> and in turn, this will inspire more people to pursue in the reaction schemes the preparation of the tungsten oxide based materials with distinct size and shape.

Tungsten oxide based materials, including tungsten oxides (WO<sub>3</sub>), tungsten suboxides (WO<sub>3-x</sub>), tungsten bronzes M<sub>x</sub>WO<sub>3</sub> (M = K<sup>+</sup>, Li<sup>+</sup>, etc.), and tungsten oxide hydrates (WO<sub>3</sub> · nH<sub>2</sub>O), are a kind of complicated materials with respect to crystal structure and thermal stability because of several structures and complicated formulas. For all of the WO<sub>3</sub> structures, they have a distorted ReO<sub>3</sub>-type consisting of a three-dimensional network of WO<sub>6</sub> octahedrons linked by their oxygen corners.<sup>22</sup> So far, the WO<sub>3</sub> nanomaterials with different morphologies such as

nanorods,<sup>23,24</sup> nanotubes,<sup>25,26</sup> nanoplates,<sup>27–30</sup> and nanoparticles<sup>11,31,32</sup> were successfully synthesized by various methods. Among various nanostructures, two-dimensional (2D) nanocrystals not only can provide active sites for catalysts and sensors but also can be used as building blocks to construct complex nanostructures. Recently, Oaki et al. realized the spontaneous conversion of a BaWO<sub>4</sub>-poly(acrylic acid) (PAA) to hexagonal WO<sub>3</sub> nanosheets via a dissolution–deposition process.<sup>27</sup> Sugahara and co-workers reported the synthesis of single-crystalline WO<sub>3</sub> nanoplates through a topochemical conversion process using lamellar tungstate-based inorganic–organic hybrids as precursors via intermediate species of H<sub>2</sub>WO<sub>4</sub> nanoplates.<sup>28</sup> Kalantar-zadeh et al. fabricated the atomically thin WO<sub>3</sub> using a three-step process, involving wet-chemical synthesis of hydrated-WO<sub>3</sub>, mechanical exfoliation of fundamental layers, and dehydration by annealing at 300 °C.<sup>29</sup> Kalantar-zadeh et al. also obtained the WO<sub>3</sub> nanoplatelets with thicknesses of less than 60 nm and lengths of 100–1000 nm by anodization at elevated temperatures in nitric acid.<sup>30</sup>

In this work, we report a novel synthesis of single-crystalline WO<sub>3</sub> nanoplates through a topochemical conversion process of the obtained H<sub>2</sub>WO<sub>4</sub> nanoplates into WO<sub>3</sub> nanoplates by a

Received: June 20, 2011

Revised: July 29, 2011

Published: August 16, 2011

size- and shape-controlled condensation process under hydrothermal condition at higher temperature (above 160 °C) or via calcination at higher temperatures in air. In addition, we also reported an ethanol sensor with high sensitivities and rapid response using single crystalline  $\text{WO}_3$  nanoplates as the active materials. The results indicate that the enhanced alcohol-sensing performance could be attributed to the plate-like morphology, especially the high crystallinity, due to the advantages of the effective adsorption and rapid diffusion of the alcohol molecules.

## 2. EXPERIMENTAL SECTION

**2.1. Synthesis.** All the chemicals were of analytical grade and used without further purification. In a typical synthesis, 0.5 g of  $\text{Na}_2\text{WO}_4 \cdot 2\text{H}_2\text{O}$  was introduced into 23.5 mL of distilled water. After  $\text{Na}_2\text{WO}_4 \cdot 2\text{H}_2\text{O}$  was completely dissolved, 1.5 mL of  $\text{HBF}_4$  solution ( $w$ , 40%) was added dropwise to the  $\text{Na}_2\text{WO}_4$  solution under magnetic stirring. After stirring for about 10 min, the above mixture was transferred into a 30 mL Teflon-lined stainless-steel autoclave. The autoclave was maintained at fixed temperature for 10 h and then cooled to room temperature naturally. The resulting product was collected by filtration, washed several times with distilled water and absolute ethanol, and then dried at 60 °C in air for 4 h.

**2.2. Characterization.** The X-ray diffraction (XRD) patterns of the products were recorded with Rigaku D/max Diffraction System using a  $\text{Cu K}\alpha$  source ( $\lambda = 0.15406$  nm). The scanning electron microscopy (SEM) images were taken with a JEOL JSM-6700F field emission scanning electron microscope (15 kV). The transmission electron microscopy (TEM) and high-resolution transmission electron microscopy (HRTEM) images were taken on a JEOL 2010 high-resolution transmission electron microscope performed at 200 kV. The specimen of HR-TEM measurement was prepared via spreading a droplet of ethanol suspension onto a copper grid, coated with a thin layer of amorphous carbon film, and allowed to dry in air.

**2.3. Fabrication and Analysis of Gas Sensor.** The gas sensor was fabricated as follows: A proper amount of  $\text{WO}_3$  nanomaterials was ground with several drops of water in an agate mortar to form a slurry. Then, the slurry was coated onto an alumina tube with a diameter of 1 mm and length of 4 mm, positioned with two Au electrodes and four Pt wires on each end of the tube. A Ni–Cr alloy filament was put through the tube and used as a heater by tuning the heating voltage. Gas sensing tests were performed on a static test system (HW-30A, HanWei Electronics Co., Ltd., Henan Province, China) using air as the reference and diluting gas at a relative humidity (RH) of 38%. The sensor was placed in a transparent testing chamber with a volume of 15 L and aged for several days before analysis. Target gas such as ethanol was injected into the testing chamber by a microsyringe. The sensor signal voltage ( $V_{\text{out}}$ ) was collected by a computer at a constant test voltage of 5 V. The sensor response is defined as the ratio  $S = R_a/R_g$ , where  $R_a$  and  $R_g$  are the electrical resistance of the sensor in test gas and in air, respectively. The response and recovery time is defined as the time for the sensor to reach 90% of its maximum response and falls to 10% of its maximum response, respectively. Photographs of the gas sensor and working principle of HW-30A system can be obtained from our previous work.<sup>33</sup>

## 3. RESULTS AND DISCUSSION

**3.1. Structure and Morphology.** We first studied how the structure and chemical composition of tungsten oxide products

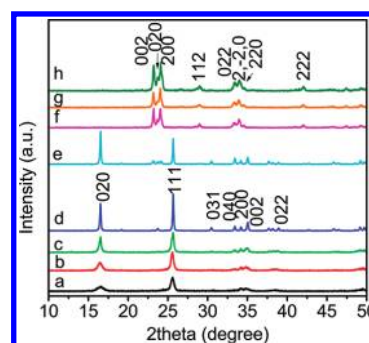
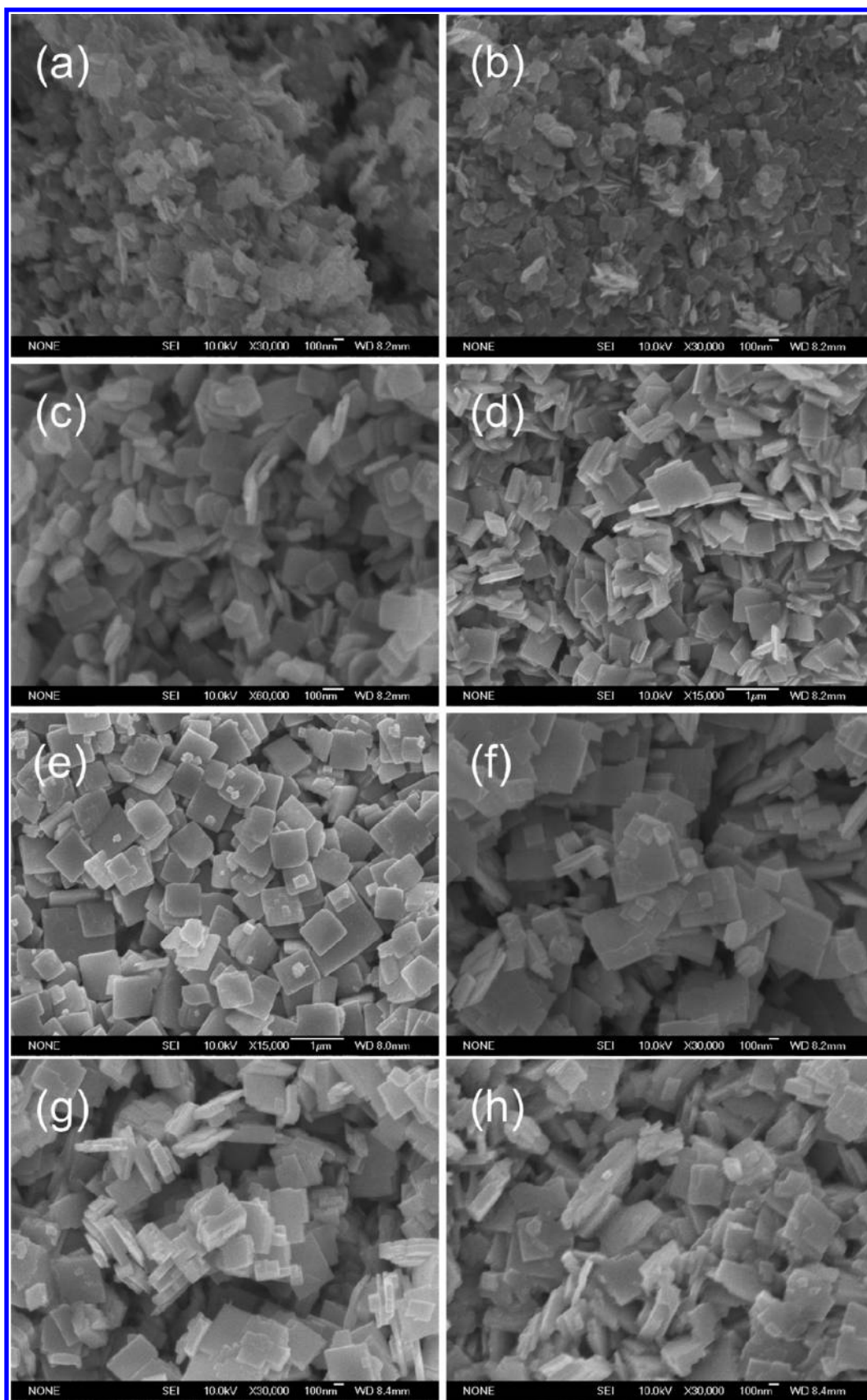


**Figure 1.** XRD patterns of the products synthesized at different temperature: (a) 30, (b) 60, (c) 90, (d) 120, (e) 150, (f) 160, (g) 180, and (h) 210 °C.

changed as the reaction temperature increased from 30 to 210 °C while keeping the other conditions constant. The XRD patterns of the samples synthesized at different temperatures are shown in Figure 1. When reactions were conducted at lower temperatures (from 30 to 90 °C), pure orthorhombic  $\text{H}_2\text{WO}_4$  phase (JCPDS No. 43-0679) could be obtained, as shown in Figure 1a–c. With the temperature increasing to the ranges from 120 to 160 °C, orthorhombic  $\text{H}_2\text{WO}_4$  and triclinic  $\text{WO}_3$  phase (JCPDS No. 32-1395) could be found to coexist, as shown in Figure 1, panels d and e. Further enhancing the reaction temperature, the crystal phase of the samples changed to pure triclinic  $\text{WO}_3$  (JCPDS No. 32-1395), which could be confirmed from the XRD results in Figure 1f–g. The above investigations showed that both pure orthorhombic  $\text{H}_2\text{WO}_4$  and triclinic  $\text{WO}_3$  phase could be obtained by varying the reaction temperatures in present studied system.

The size and shape of the as-synthesized products were further analyzed by SEM technique. Figure 2 shows the representative SEM images of the samples synthesized at different temperatures. It is observed that all of the products are composed of a large quantity of nanoplates. The sizes of nanoplates obviously increase with an increase in the reaction temperature. In addition, it should be noted that the homogeneity of samples becomes lower with an increase in the reaction temperature. Our results indicate that the reaction temperature plays an important role in controlling nucleation and growth of tungsten oxide nanoplates. An appropriate temperature is critical for the nanoplates with different composition and size. In order to clearly illustrate the temperature-dependent chemical components, size and shape of final products, the detailed conditions for preparing some typical samples are listed in Table 1.

To further investigate the detailed structural and morphological characteristics of tungsten oxides, we chose the three typical samples (P-60, P-120, and P-180) as studied targets and investigated them by transmission electron microscopy (TEM) technique. Figure 3 shows the TEM observations of the samples (P-60, P-120, and P-180) synthesized at different temperatures, respectively. Figure 3a shows a low magnification TEM image of P-60, which presents a quadrangular plate-like morphology with a side length of 120–180 nm. In addition, it is clear that these  $\text{H}_2\text{WO}_4$  nanoplates have a very low thickness. In Figure 3b, the HR-TEM image of an individual  $\text{H}_2\text{WO}_4$  nanoplate reveals that the as-synthesized  $\text{H}_2\text{WO}_4$  (P-60) is not well crystalline. It should be noted that there also are some defects in the  $\text{WO}_3$  nanoplate, as marked by a circle in Figure 3b. The corresponding local fast Fourier transform (FFT) pattern (the inset of Figure 3b)

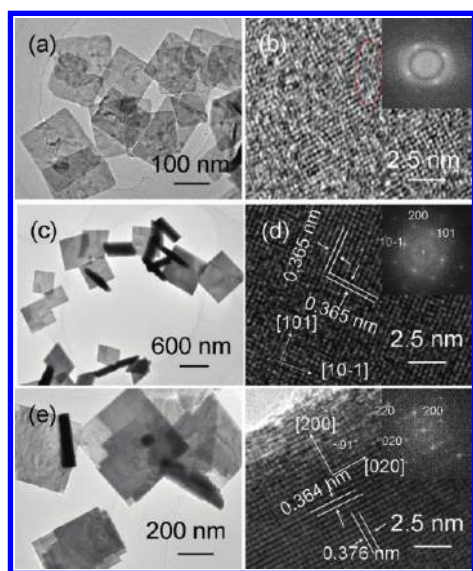


**Figure 2.** SEM images of the products synthesized at different temperature: (a) 30, (b) 60, (c) 90, (d) 120, (e) 150, (f) 160, (g) 180, and (h) 210 °C.

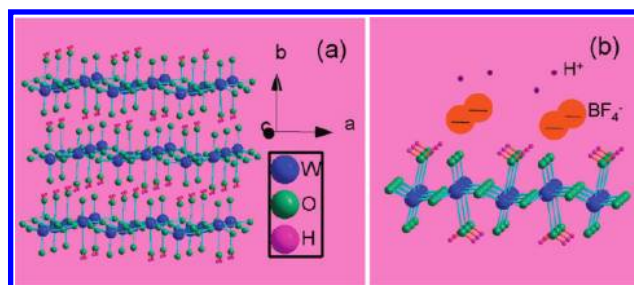


**Table 1.** Experimental Condition for the Preparation of Samples

sample no.	temperature (°C)	phase	morphology	size (nm)
P-30	30	<i>o</i> -H <sub>2</sub> WO <sub>4</sub>	nanoplates	100–130
P-60	60	<i>o</i> -H <sub>2</sub> WO <sub>4</sub>	nanoplates	100–130
P-90	90	<i>o</i> -H <sub>2</sub> WO <sub>4</sub>	nanoplates	80–130
P-120	120	<i>o</i> -H <sub>2</sub> WO <sub>4</sub> and <i>t</i> -WO <sub>3</sub>	nanoplates	500–1000
P-150	150	<i>o</i> -H <sub>2</sub> WO <sub>4</sub> and <i>t</i> -WO <sub>3</sub>	nanoplates	500–1200
P-160	160	<i>t</i> -WO <sub>3</sub>	nanoplates	400–1000
P-180	180	<i>t</i> -WO <sub>3</sub>	nanoplates	200–1000
P-210	210	<i>t</i> -WO <sub>3</sub>	nanoplates	100–700

**Figure 3.** (a) TEM images and (b) HR-TEM image of P-60; (c) TEM images and (d) HR-TEM image of P-120; (e) TEM images and (f) HR-TEM image of P-180.

of P-60 further indicates its polycrystalline nature. Figure 3, panels c and d, shows the TEM and HR-TEM images of H<sub>2</sub>WO<sub>4</sub> nanoplates (P-120), respectively. Figure 3a shows a low magnification TEM image of P-120, which presents a quadrangular plate-like morphology with a side length of 450–600 nm and a thickness of about 50 nm. In Figure 3d, a clear 2D crystal lattice is revealed, and the interplanar distances of 0.365 and 0.365 nm can be readily assigned to the 101 and 10 $\bar{1}$  crystal planes, respectively. The separation angle of the [101] and [10 $\bar{1}$ ] directions is 88.9°, which is extremely close to the calculated value according to the cell parameters. Based on the above analyses, it can be concluded that the single-crystalline orthorhombic H<sub>2</sub>WO<sub>4</sub> nanoplates synthesized at 120 °C are perpendicular to the *c* axis. Figure 3e shows a typical TEM image of WO<sub>3</sub> (P-180), which consists of nanoplates with different sizes, and the thickness of the nanoplates is about 50 nm. The HR-TEM image obtained from the central part of the nanoplate (Figure 3e) is presented in Figure 3f. It also shows a clear 2D crystal lattice, the interplanar distances of 0.364 and 0.376 nm of which can be readily assigned to the 200 and 020 crystal planes, respectively. The separation angle of the [200] and [020] directions is about 91°, which is extremely close to the value of the triclinic WO<sub>3</sub> phase. The HR-TEM image

**Figure 4.** Schematic illustrations: (a) the H<sub>2</sub>WO<sub>4</sub> crystal structure and (b) the interaction of H<sub>2</sub>WO<sub>4</sub> crystal planes and HBF<sub>4</sub>.

and FFT pattern (Figure 3f) indicate that the WO<sub>3</sub> nanoplate derived from the H<sub>2</sub>WO<sub>4</sub> nanoplate is a whole single crystal.

**3.2. Formation Mechanism of H<sub>2</sub>WO<sub>4</sub> and WO<sub>3</sub> Nanoplates.** Usually, there are many factors that influence the morphology of the nanocrystals, such as crystal growth habits and external factors. The intrinsic crystal structure is the essential factor for morphology control. Here, to discuss the formation mechanism of orthorhombic H<sub>2</sub>WO<sub>4</sub> nanoplates, its crystal structure is given in Figure 4a and depicted as follows: it consists of layers of [WO<sub>6</sub>] octahedra, which share their four equatorial oxygen atoms. The layers are linked to each other through hydrogen bonds, which are derived from the interaction of water molecules and oxygen atoms in the axial positions of [WO<sub>6</sub>] octahedra with the neighboring layers. The normal direction of the layers of [WO<sub>6</sub>] octahedra is the crystal direction [010]. Because of the lamellar structure separated by crystal water molecules along the (010) crystal plane, H<sub>2</sub>WO<sub>4</sub> tends to form plate-like nanocrystals with an inhibited growth direction of [010].

On the other hand, the external environment can also remarkably influence the growth of nanocrystals, for example, the kinetics of nucleation and crystal growth. In the present case, the formation of H<sub>2</sub>WO<sub>4</sub> nanoplates indicated that the nucleation and growth were well controlled by using HBF<sub>4</sub> as the acid source. The BF<sub>4</sub><sup>−</sup> anion has a distorted tetrahedron structure, in which four fluorine atoms occupy the apexes of a tetrahedron centering on each boron atom. BF<sub>4</sub><sup>−</sup> anion can be added to the hydrogen bonds system, which may induce the oriented arrangement of the BF<sub>4</sub><sup>−</sup> anion on the (010) plane of H<sub>2</sub>WO<sub>4</sub>. Thus, the growth of the (010) plane of H<sub>2</sub>WO<sub>4</sub> is inhibited by the adsorption of BF<sub>4</sub><sup>−</sup> anions, and H<sub>2</sub>WO<sub>4</sub> nanoplates are produced. A similar phenomenon for the synthesis of turbostratic boron nitride (BN) nanoplates has been reported by our group.<sup>34</sup> In order to clearly demonstrate the interaction of H<sub>2</sub>WO<sub>4</sub> crystal planes and HBF<sub>4</sub>, a schematic illustration is given in Figure 4b.

Furthermore, in order to explain the formation mechanism of triclinic WO<sub>3</sub> nanoplates, we first studied the structure and morphology of intermediate products at different times. In Figure 5, one can see that the final triclinic WO<sub>3</sub> (Figure 5d) is evolved from the initial orthorhombic H<sub>2</sub>WO<sub>4</sub> (Figure 5b) from XRD data (Figure 5a–d). In addition, the morphology evolution experiments (Figure 6a–d) indicate that the final triclinic WO<sub>3</sub> nanoplates (Figure 6d) is from the H<sub>2</sub>WO<sub>4</sub> nanoplates (Figure 6b) with the same size derived from the Ostwald ripening process of the initial small H<sub>2</sub>WO<sub>4</sub> nanoplates (Figure 6a). It should be noted that the coexistence of H<sub>2</sub>WO<sub>4</sub> and WO<sub>3</sub> (Figure 5c) and the morphological similarity (Figure 6b–d) further demonstrate the transformation process of WO<sub>3</sub> nanoplates from H<sub>2</sub>WO<sub>4</sub>. Both the similar dimensionalities (Figure 6) and phase change

(Figure 5) verify that the condensation from  $\text{H}_2\text{WO}_4$  nanoplates to  $\text{WO}_3$  nanoplates is a topotactic process. In addition, the similarity between the orthorhombic  $\text{H}_2\text{WO}_4$  and triclinic  $\text{WO}_3$  in the crystal structure may play essential roles during the topotactic process. Further studies are still necessary to understand their growth process, which can provide important information for structure design and morphology controlled synthesis of oxides.

**3.3. Influence of Calcination Temperature on the Structure and Morphology.** According to the above discussion for the formation mechanism of  $t\text{-WO}_3$  and other literature,<sup>12,27–30</sup> the crystal water molecules in  $\text{H}_2\text{WO}_4$  nanoplates can be readily removed by annealing them at an elevated temperature. Herein, in order to investigate the gas-sensing properties, the P-60 and P-120 samples were selected as precursors and then annealed at

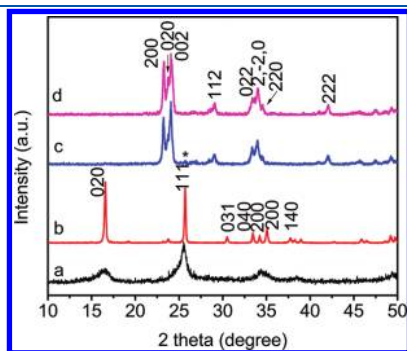
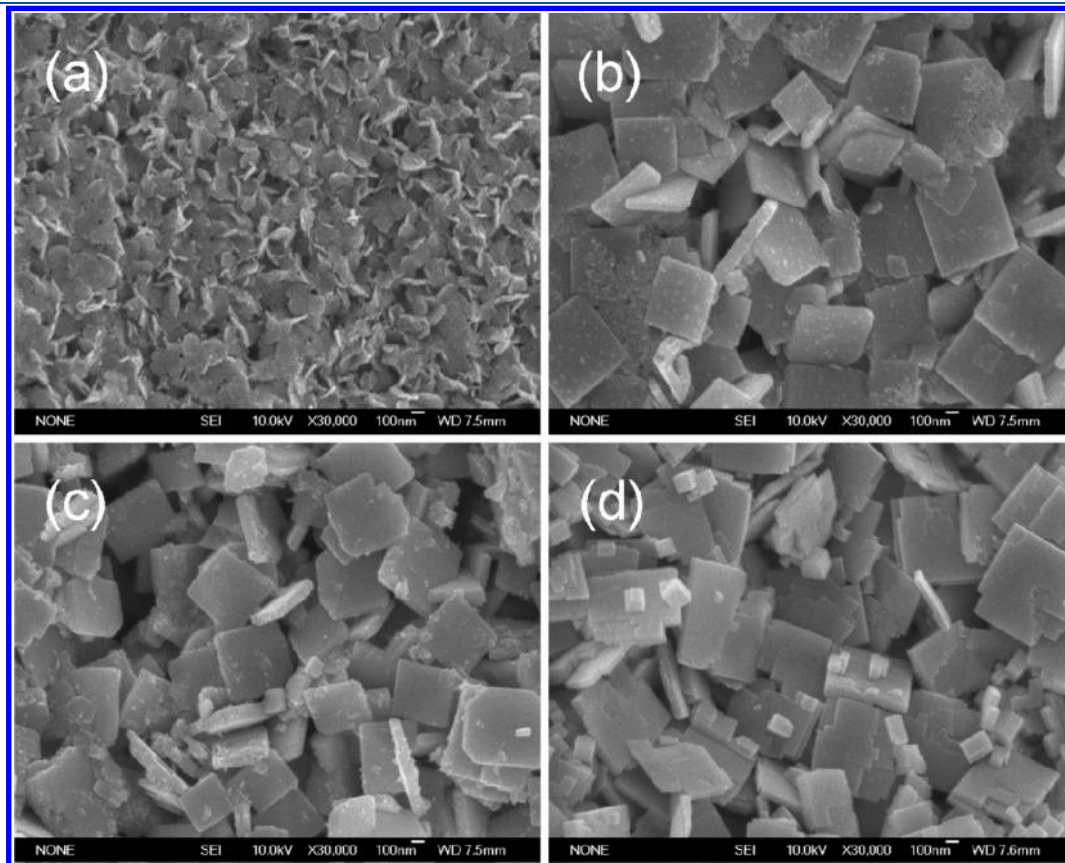


**Figure 5.** XRD patterns of the products synthesized for different times at 180 °C: (a) 10 min, (b) 1 h, (c) 2.5 h, and (d) 5 h.

various temperatures in air for 2 h. The as-obtained results are listed in Table 2.

Figure 7 shows the typical XRD patterns of the products calcined at various temperatures of 300–600 °C in air for 2 h. All of the diffraction peaks in the patterns can readily be indexed to a pure triclinic phase [space group  $P\bar{1}(2)$ ] of  $\text{WO}_3$  phase (JCPDS No. 32-1395). No  $\text{H}_2\text{WO}_4$  is observed, implying the precursors have been completely converted into  $t\text{-WO}_3$  via heat treatment. In addition, with increases in calcination temperatures from 300 to 600 °C, the diffraction peaks in Figure 7 for  $\text{WO}_3$  nanocrystals gradually become sharp, suggesting enhancement in the degree of dehydration and reorganization during the calcination process.

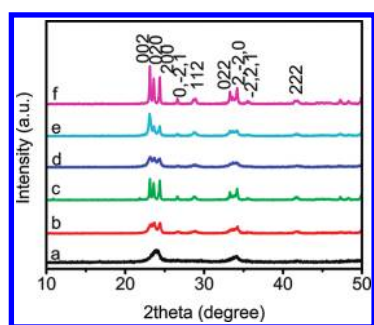
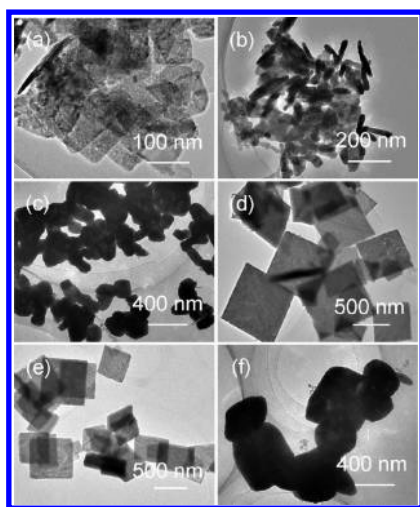
Figure 8 shows the TEM images of P-60 and P-120 calcined in air at different temperatures for 2 h, respectively. For products S1–S3 calcined from the precursor P-60, it is found that only the plate-like morphology of S4 calcined at 300 °C (Figure 8a) was essentially preserved in the process of calcination. When the annealing temperatures were increased to relative high temperatures (450 and 600 °C), the morphologies of the samples completely changed, which consisted of interconnected nanocrystallites (Figure 8b and c). For products S4–S6 calcined from the precursor P-120, one can find that the plate-like morphology (Figure 8d and e) is still maintained until the calcining temperature reached 450 °C. However, the sharp angles of the nanoplates gradually become rounder after calcining P-120 at 600 °C, as shown in Figure 8f. The above result suggests that crystal growth and atom rearrangement occur at the sharp edges due to their high energy levels when calcining the samples at an elevated temperature. In addition, it should be noted that only the thicker  $\text{WO}_3$  nanoplates can easily maintain the plate-like morphology at higher temperature.



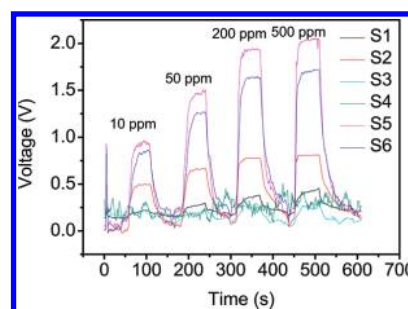
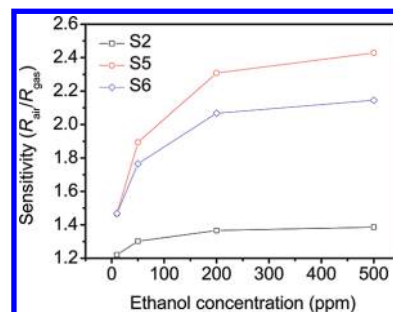
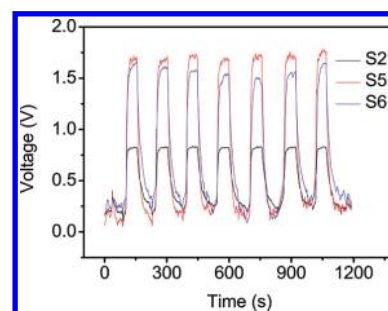
**Figure 6.** SEM images of the products synthesized for different times at 180 °C: (a) 10 min, (b) 1 h, (c) 2.5 h, and (d) 5 h.

**Table 2. Results and Experimental Parameters for the Annealed Samples at Different Temperatures**

sample no.	precursor	annealing temperature (°C)	phase	morphology
S1	P-60	300	<i>t</i> -WO <sub>3</sub>	nanoplates
S2	P-60	450	<i>t</i> -WO <sub>3</sub>	nanoparticles
S3	P-60	600	<i>t</i> -WO <sub>3</sub>	nanoparticles
S4	P-120	300	<i>t</i> -WO <sub>3</sub>	nanoplates
S5	P-120	450	<i>t</i> -WO <sub>3</sub>	nanoplates
S6	P-120	600	<i>t</i> -WO <sub>3</sub>	nanoplates

**Figure 7.** XRD patterns of the different samples: (a) S1, (b) S2, (c) S3, (d) S4, (e) S5, and (f) S6.**Figure 8.** (a) TEM image of S1. (b) TEM image of S2. (c) TEM image of S3. (d) TEM image of S4. (e) TEM image of S5. (f) TEM image of S6.

**3.4. Performances of WO<sub>3</sub> Nanomaterials Gas Sensor.** First of all, we use the S1–S6 as the active element for evaluating the alcohol-sensing properties of single crystalline WO<sub>3</sub> nanomaterials, respectively. Figure 9 shows the dynamic responses of the WO<sub>3</sub> nanomaterials at the operating temperature of 300 °C with various concentrations of alcohols. It can be seen that the S5 sensor is more sensitive than the others. The response amplitude of the S2, S5, and S6 sensors are increased with increasing ethanol concentration, whereas the increase in the response of the S1, S3, and S4 sensors is almost negligible. Sensitivity is another important factor of chemical sensors; a higher sensitivity can usually allow for a lower detection limit.<sup>35</sup> The sensor sensitivities to different ethanol concentrations are compared in Figure 10, showing that the sensor sensitivity for all of the sensors (S2, S5, and S6) is

**Figure 9.** Dynamic response-recovery curves of the six sensors to different ethanol concentrations.**Figure 10.** Comparison of sensor sensitivities to different ethanol concentrations for different catalysts.**Figure 11.** Reproducibility of the WO<sub>3</sub> sensors on successive exposure (7 cycles) to 100 ppm ethanol.

improved with increasing gas concentration. In Figure 10, the WO<sub>3</sub> (S5) sensor has much higher sensitivities, and its sensor sensitivity is further largely improved with increasing gas concentration due to the high crystallinity and plate-like morphology of S5. Finally, it should be noted that WO<sub>3</sub> (S2, S5, and S6) sensors have excellent reproducibility. As shown in Figure 11, the reproducibility experiment of the WO<sub>3</sub> (S2, S5, and S6) sensors demonstrate that the sensor maintains its initial response amplitude without a clear decrease upon seven successive sensing tests to 100 ppm ethanol. These results demonstrate that the WO<sub>3</sub> (S5) sensor has higher sensitivities and a faster response on ethanol as well as good stability due to its plate-like morphology and high crystallinity.<sup>12</sup>

For common n-type semiconductors, their sensing mechanism generally can be interpreted by the classical electron depletion theory.<sup>36,37</sup> For example, the surface of SnO<sub>2</sub> is depleted of electrons by the absorbed oxygen species (O<sub>2</sub><sup>2-</sup>, O<sub>2</sub><sup>-</sup>, and O<sup>-</sup>) from the conduction band of SnO<sub>2</sub>, resulting in a high resistance



of the sensor.<sup>38</sup> In this work, surface sensing reactions maybe happen on the surface of WO<sub>3</sub> nanoplates, when the WO<sub>3</sub> nanoplates are exposed to a reducing gas such as ethanol. The ethanol molecules can be oxidized by the surface absorbed oxygen species (O<sup>2-</sup>, O<sub>2</sub><sup>-</sup> and O<sup>-</sup>) and consequently, the depleted electrons will be released to WO<sub>3</sub>. However, there is another “generation of oxygen vacancies” model suggested by Georg et al.,<sup>39</sup> which also can be used to explain the origin of the surface oxygen vacancies of WO<sub>3</sub>. The model involves following steps: H atoms were dissociated from the absorbed ethanol on the surface, and then these H atoms reacted with the lattice oxygen of the WO<sub>3</sub> film, which ultimately created surface oxygen vacancies and adsorbed water molecules.<sup>39,40</sup> Thus, the gas sensing mechanism of WO<sub>3</sub> toward ethanol needs further investigation. Finally, it should be noted that the unique plate-like morphology of WO<sub>3</sub> should be highly advantageous for the gas sensing reaction, as it has a large exposure of surface atoms providing more active sites for the absorption of gas molecules and hence promoting the surface reactions.

#### 4. CONCLUSION

In summary, we have developed a facile solution phase route to the single-crystalline WO<sub>3</sub> nanoplates through a topochemical conversion process of the obtained H<sub>2</sub>WO<sub>4</sub> nanoplates into WO<sub>3</sub> nanoplates by a size- and shape-controlled condensation process under hydrothermal condition at higher temperature (above 160 °C) or via calcination at higher temperatures in air. This synthetic method is simple, mild, and controllable, and it provides a novel method for direct solution growth of highly oriented two-dimensional nanostructures. The formation of nanoplates of H<sub>2</sub>WO<sub>4</sub> is closely related to that of fluoroboric acid due to its unique structure. Furthermore, it was found that the gas-sensing performance could be improved by choosing the plate-like morphology and high crystallinity of *t*-WO<sub>3</sub> nanoplates in aspects of the high sensitivities and rapid response on ethanol due to the advantages of the effective adsorption and rapid diffusion of the alcohol molecules.

#### AUTHOR INFORMATION

##### Corresponding Author

\*E-mail: zhwj@nankai.edu.cn.

#### ACKNOWLEDGMENT

This work was financially supported by the National Natural Science Foundation of China (20971070 and 21073095) and MOE (No. RT0927).

#### REFERENCES

- (1) Ma, J. M.; Duan, X. C.; Lian, J. B.; Kim, T. I.; Peng, P.; Liu, X. D.; Liu, Z. F.; Li, H. B.; Zheng, W. J. *Chem.—Eur. J.* **2010**, *16*, 13210–13217.
- (2) Ma, J. M.; Chang, L.; Lian, J. B.; Huang, Z.; Duan, X. C.; Liu, X. D.; Peng, P.; Kim, T. I.; Liu, Z. F.; Zheng, W. J. *Chem. Commun.* **2010**, *46*, S006–S008.
- (3) Pan, W. Z.; Tian, R. Y.; Jin, H.; Guo, Y. J.; Zhang, L. P.; Wu, X. C.; Zhang, L. N.; Han, Z. H.; Liu, G. Y.; Li, J. B.; Rao, G. H.; Wang, H. F.; Chu, W. G. *Chem. Mater.* **2010**, *22*, 6202–6208.
- (4) Vallejos, S.; Stoycheva, T.; Umek, P.; Navio, C.; Snyders, R.; Bittencourt, C.; Llobet, E.; Blackman, C.; Moniz, S.; Correig, X. *Chem. Commun.* **2011**, *47*, S65–S67.
- (5) Zhu, J. H.; Wei, S. Y.; Alexander, M.; Dang, T. D.; Ho, T. C.; Guo, Z. H. *Adv. Funct. Mater.* **2010**, *20*, 3076–3084.

- (6) Blackman, C. S.; Parkin, I. P. *Chem. Mater.* **2005**, *17*, 1583–1590.
- (7) Figueroa, R.; Kleinke, M.; Cruz, T. G. S.; Gorenstein, A. J. *Power Sources* **2006**, *162*, 1351–1356.
- (8) Li, W. J.; Fu, Z. W. *Appl. Surf. Sci.* **2010**, *256*, 2447–2452.
- (9) Miseki, Y.; Kusama, H.; Sugihara, H.; Sayama, K. J. *Phys. Chem. Lett.* **2010**, *1*, 1196–1200.
- (10) Sayama, K.; Hayashi, H.; Arai, T.; Yanagida, M.; Gunji, T.; Sugihara, H. *Appl. Catal. B: Environ.* **2010**, *94*, 150–157.
- (11) Ardizzone, S.; Cappelletti, G.; Ricci, C.; Sin, A. J. *Nanosci. Nanotechnol.* **2010**, *10*, 8367–8374.
- (12) Chen, D. L.; Hou, X. X.; Wen, H. J.; Wang, Y.; Wang, H. L.; Li, X. J.; Zhang, R.; Lu, H. X.; Xu, H. L.; Guan, S. K.; Sun, J.; Gao, L. *Nanotechnology* **2010**, *21*, 035501.
- (13) Khatko, V.; Vallejos, S.; Calderer, J.; Gracia, I.; Cane, C.; Llobet, E.; Correig, X. *Sens. Actuators B* **2009**, *140*, 356–362.
- (14) Liu, H. J.; Huang, S. J.; Zhang, L.; Liu, S. L.; Xin, W. J.; Xu, L. Y. *Catal. Commun.* **2009**, *10*, S44–S46.
- (15) Gondal, M. A.; Hameed, A.; Yamani, Z. H. *J. Mol. Catal. A-Chem.* **2004**, *222*, 259–264.
- (16) Zheng, H. D.; Tachibana, Y.; Kalantar-zadeh, K. *Langmuir* **2010**, *26*, 19148–19152.
- (17) Meda, L.; Tozzola, G.; Tacca, A.; Marra, G.; Caramori, S.; Cristino, V.; Bignozzi, C. A. *Sol. Energy Mater. Sol. Cells* **2010**, *94*, 788–796.
- (18) Li, Y. B.; Bando, Y.; Golberg, D. *Adv. Mater.* **2003**, *15*, 1294–1298.
- (19) Liu, J. G.; Zhang, Z. J.; Zhao, Y.; Su, X.; Liu, S.; Wang, E. G. *Small* **2005**, *1*, 310–313.
- (20) Granqvist, C. G. *Sol. Energy Mater. Sol. Cells* **2000**, *60*, 201–262.
- (21) Zheng, H. D.; Ou, J. Z.; Strano, M. S.; Kaner, R. B.; Mitchell, A.; Kalantar-zadeh, K. *Adv. Funct. Mater.* **2011**, *21*, 2175–2196.
- (22) Guery, C.; Choquet, C.; Dujeancourt, F.; Tarascon, J. M.; Lassegues, J. C. *J. Solid State Electrochem.* **1997**, *1*, 199–207.
- (23) Wang, J. M.; Khoo, E.; Lee, P. S.; Ma, J. J. *Phys. Chem. C* **2008**, *112*, 14306–14312.
- (24) Phuruangrat, A.; Ham, D. J.; Hong, S. J.; Thongtem, S.; Lee, J. S. *J. Mater. Chem.* **2010**, *20*, 1683–1690.
- (25) Wang, Z. X.; Zhou, S. X.; Wu, L. M. *Adv. Funct. Mater.* **2007**, *17*, 1790–1794.
- (26) Chen, D.; Sugahara, Y. *Chem. Mater.* **2007**, *19*, 1808–1815.
- (27) Oaki, Y.; Imai, H. *Adv. Mater.* **2006**, *18*, 1807–1811.
- (28) Chen, D.; Gao, L.; Yasumori, A.; Kuroda, K.; Sugahara, Y. *Small* **2008**, *4*, 1813–1822.
- (29) Kalantar-zadeh, K.; Vijayaraghavan, A.; Ham, M.; Zheng, H. D.; Breedon, M.; Strano, M. S. *Chem. Mater.* **2010**, *22*, S660–S666.
- (30) Sadek, A. Z.; Zheng, H. D.; Breedon, M.; Bansal, V.; Bhargava, S. K.; Latham, K.; Zhu, J. M.; Yu, L. S.; Hu, Z.; Spizzirri, P. G.; Wlodarski, W.; Kalantar-zadeh, K. *Langmuir* **2009**, *25*, 9545–9551.
- (31) Le Houx, N.; Pourroy, G.; Camerel, F.; Comet, M.; Spitzer, D. *J. Phys. Chem. C* **2010**, *114*, 151–161.
- (32) Heidari, E. K.; Marzbanrad, E.; Zamani, C.; Raissi, B. *Nanoscale Res. Lett.* **2010**, *5*, 370–373.
- (33) Zhang, J.; Wang, S. R.; Xu, M. J.; Wang, Y.; Zhu, B. L.; Zhang, S. M.; Huang, W. P.; Wu, S. H. *Cryst. Growth Des.* **2009**, *9*, 3532–3537.
- (34) Lian, J. B.; Kim, T. I.; Liu, X. D.; Ma, J. M.; Zheng, W. J. *J. Phys. Chem. C* **2009**, *113*, 9135–9140.
- (35) Zhang, J.; Liu, X. H.; Guo, X. Z.; Wu, S. H.; Wang, S. R. *Chem.—Eur. J.* **2010**, *16*, 8108–8116.
- (36) Williams, D. E. *Sens. Actuators B: Chem.* **1999**, *57*, 1–16.
- (37) Barsan, N.; Weimar, U. J. *J. Electroceram.* **2001**, *7*, 143–167.
- (38) Ma, J. M.; Zhang, J.; Wang, S. R.; Yang, J. Q.; Wang, Q. H.; Jiao, L. F.; Duan, X. C.; Lian, J. B.; Liu, Z. F.; Kim, T. I.; Zheng, W. J. *CrystEngComm* DOI: 10.1039/c1ce05320e.
- (39) Georg, A.; Graf, W.; Neumann, R.; Wittwer, V. *Solid State Ionics* **2000**, *127*, 319–328.
- (40) Ou, J. Z.; Yaacob, M. H.; Breedon, M.; Zheng, H. D.; Campbell, J. L.; Latham, K.; du Plessis, J.; Wlodarski, W.; Kalantar-zadeh, K. *Phys. Chem. Chem. Phys.* **2011**, *13*, 73330–7339.